Journal of Alloys and Compounds 905 (2022) 164225

Contents lists available at ScienceDirect

Journal of Alloys and Compounds

journal homepage: www.elsevier.com/locate/jalcom

Research article

Magnetism and magnetic structure determination of a selected $(Mn,Co)_{23}B_6$-compound

Simon R. Larsen[a,*], Daniel Hedlund[b], Rebecca Clulow[a], Martin Sahlberg[a], Peter Svedlindh[b], Erna K. Delczeg-Czirjak[c], Johan Cedervall[d,e]

[a] Department of Chemistry - Ångström Laborator, Uppsala University, Box 538, 751 21 Uppsala, Sweden
[b] Department of Materials Science and Engineering, Uppsala University, Box 35, 751 03 Uppsala, Sweden
[c] Department of Physics and Astronomy, Uppsala University, Box 516, 751 20 Uppsala, Sweden
[d] Department of Materials and Environmental Chemistry, Stockholm University, 10691 Stockholm, Sweden
[e] ISIS Pulsed Neutron & Muon Facility, Rutherford Appleton Laboratory, Harwell Campus, OX11 0QX, United Kingdom

ARTICLE INFO

Article history:
Received 10 December 2021
Received in revised form 24 January 2022
Accepted 12 February 2022
Available online 16 February 2022

Keywords:
Magnetism
X-ray diffraction
Neutron diffraction
First principles calculations

ABSTRACT

The vast compositional space in cubic $Cr_{23}C_6$-type compounds (space group $Fm\bar{3}m$) opens up possibilities to tune properties by performing substitutions. In this study, the magnetic properties have been explored in a selected $(Mn,Co)_{23}B_6$-compound by the means of synchrotron X-ray diffraction, neutron powder diffraction, magnetometry and electronic structure calculations. Refinements of a structural model based on combined X-ray and neutron diffraction data revealed mixed metal occupancies at all metal positions. However, two sites were richer in Co and the other two showed an abundance of Mn. The magnetic characteristics showed a ferrimagnetic structure below 550 K, with the magnetic moments aligned along the crystallographic *c*-direction and the magnetic moments on corner atoms having an opposite direction compared to the rest, within the magnetic space group $I4/mm'm'$. The total magnetic moments extracted from magnetometry and neutron diffraction data gave similar values at 6 K, 20.1 and 18.2 μ_B/f.u., respectively. Results from electronic structure calculations are in reasonable agreement with the experimental findings.

1. Introduction

Magnetic materials are a crucial component in numerous devices in the modern society, e.g., windmills for sustainable energy production and electric motors. The use of magnetic materials is expected to grow continuously as the world is becoming ever more aware of the effects of climate change. There is a continuous need to develop new magnetic materials based on transition metals, to replace the rare-earth-containing alloys which are dominating the market for high-performance magnets today. Especially manganese containing compounds are interesting given the low cost of manganese and the potential for a high magnetic moment of its alloys [1]. One issue with manganese in its pure form is that it orders antiferromagnetically, so alloying is necessary to transform the magnetic interactions to ferromagnetic. In this paper, we report on the structure-property relations in a Mn-Co-B alloy and determine its magnetic structure to provide insight into how best to harness the magnetic properties of Mn.

$Cr_{23}C_6$ is a compound often found in steels and has interesting crystallographic properties [2]. The compound crystallizes within the cubic structure, space group (SG) $Fm\bar{3}m$, with a unit cell parameter of $a = 10.638$ Å. The C-atoms occupy the 24*e* position, whereas Cr is divided between the 4*a*, 8*c*, 32*f* and 48*h* positions, giving a total of 116 atoms per unit cell, i.e., 4 formula units. The atomic structure is visualized in Figure 1. There is a vast compositional space available given the number of crystallographic sites that can be separated and occupied by one atom type, or mixed by several atoms. This gives possibilities of ordered and disordered compounds while still retaining the $Fm\bar{3}m$ crystal symmetry.

Upon generalization of the $Cr_{23}C_6$-type structure to $M_{23}X_6$ [3] or $M_{23-x}M'_xX_6$ [4], with e.g., M = Co, Fe, Ni, M' = Al, Mn and X = B, C, P, the chemical freedom within this structure becomes apparent. For $Ni_{23-x}Al_xB_6$ the effects on the unit cell parameter were evaluated with respect to the Al content [5]. Since several magnetic elements can occupy the metal positions within the $Cr_{23}C_6$-type structure, interesting magnetic properties can be found in these materials. Examples of this are found in the $Al_3(Co,Fe,Ni)_{20}B_6$-system. There the ferromagnetic moments per unit cell as well as the Curie transition temperature, T_C, are tuneable with composition. The highest values

* Corresponding author.
E-mail address: simon.rosenqvist.larsen@kemi.uu.se (S.R. Larsen).

https://doi.org/10.1016/j.jallcom.2022.164225

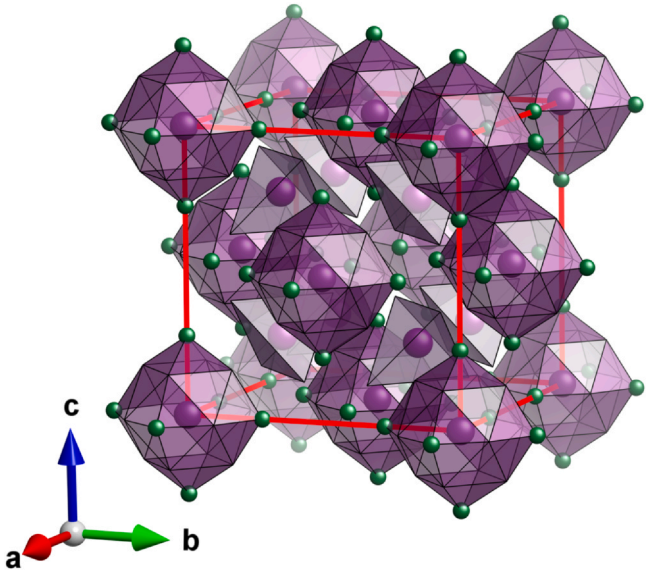

Fig. 1. Structural model for $Cr_{23}C_6$ with C shown in green and Cr in purple, with coordination polyhedra for the 4*a* and 8*c* positions in darker and lighter purple, respectively. The Cr in the 32*f*-positions is on the corner of the tetrahedra surrounding 8*c* whereas the 48*h*-positions are occupying the empty corners of the 4*a* polyhedra.

are found for $Al_3Fe_{20}B_6$ and decreases with Co-substitutions. The fully Ni-substituted compound, $Al_3Ni_{20}B_6$, is a Pauli paramagnet at least down to 77 K [6].

Another set of isostructural compounds are the Mn_3 $M_{20}P_6$ (*M* = Ni and Pd) systems [7–9]. In these compounds the magnetic moments are only dependent on the Mn atoms which are located on the 4*a* and 8*c* sites, and the distance between those atoms is essential for the magnetic properties. $Mn_3Pd_{20}P_6$ has a larger unit cell parameter than $Mn_3Ni_{20}P_6$, 11.9563(2) Åand 11.0820(2) Å, respectively, which gives a ferromagnetic structure for $Mn_3Pd_{20}P_6$ [8]. The magnetic interactions in $Mn_3Ni_{20}P_6$ are, however, more complex [9]. $Mn_3Ni_{20}P_6$ has three antiferromagnetic (AFM) transitions, where the two Mn positions order independently of each other at 240 K (4*a* position) and 30 K (8*c* position). The third AFM transition occurs at 25 K and gives an incommensurate helical arrangement on both Mn sites. Similar AFM interactions with independent ordering on the 4*a* and 8*c* sites have also been observed within $RE_3Ni_{20}X_6$ (*RE* = rare earth element, *X* = Ge, Si) compounds [10–13].

Given the number of atomic sites in the $Cr_{23}C_6$-structure several possible compounds with varying compositions can occur by just using three constituting elements. Just considering Mn, Co and B, there are several compounds reported with different stoichiometry, e.g. $Mn_3Co_{20}B_6$ [14], $Mn_2Co_{21}B_6$ [15] and $Mn_7Co_{16}B_6$ [16]. These three compounds are reported to have Mn fully occupying the 8*c*-site, and mixed occupancies of Co and Mn on the other metal positions to yield the desired stoichiometry. The unit cell parameter varies between 10.518 Åand 10.588 Åfor these different compositions. The magnetic properties of the compounds within the $(Mn,Co)_{23}B_6$-family are yet unexplored. Therefore, this study aims to explore the magnetic properties of a specific compound with the nominal composition $Mn_3Co_{20}B_6$. This has been done using a combination of synchrotron X-ray diffraction, neutron powder diffraction, magnetometry and electronic structure calculations, to fully understand the structural (nuclear and magnetic) and magnetic behavior of this compound.

2. Experimental

2.1. Synthesis

Stoichiometric quantities of powdered Co (Goodfellow, 99.9%), Mn (Goodfellow, 99.5%) and isotopically pure ^{11}B (Eagle Picher, 99.52%) were manually mixed together using a pestle and mortar. The mixture was placed in an Al_2O_3 crucible which was capped with Al_2O_3-wool. The crucible was sealed in an evacuated quartz-glass ampule and the sample was sintered at 1273 K for 2 days. Following confirmation of the structure using in-house X-ray diffraction, the sample was resealed in another evacuated ampule and annealed for an additional 12 h at 1273 K.

2.2. Diffraction

To elucidate the structural aspects of the sample both synchrotron radiation X-ray powder diffraction (XRD) and neutron powder diffraction (NPD) measurements were utilized. The X-ray diffraction measurements were performed at the P02.1 beamline at DESY in Hamburg, Germany [17]. Using a LaB_6-standard the wavelength was determined to 0.20710 Åand a PerkinElmer XRD1621 detector was used with an exposure time of 5 s per diffraction pattern during the experiments. The sample was mounted in a quartz tube and placed in a sample cell [18] connected to a vacuum pump and argon gas. The sample was heated from room temperature up to 700 K at a rate of 12 K/min. The collected 2D diffraction patterns were azimuthally integrated to 1D patterns using the software Fit2D [19]. The neutron diffraction experiments were performed using the instrument Wish at ISIS in Didcot, UK [20]. The sample was placed in a vanadium can and measured in a temperature range between 6 and 700 K [21]. All diffraction patterns were then investigated using the Rietveld method [22] implemented in the software FullProf [23]. In the refinements, the Thompson-Cox-Hastings pseudo-Voigt and the T.O.F. convolution pseudo-Voigt profile functions were used for the XRD and NPD data, respectively, to describe the peak shapes, and the background was described by interpolation between chosen points. When determining the possible magnetic space groups to describe the magnetic arrangement in $Mn_3Co_{20}B_6$ the tool k-SUBGROUPSMAG [24] from the Bilbao Crystallographic Server (BCS) was utilized. All crystal structures were visualized using the software VESTA [25].

2.3. Elemental analysis

The composition and homogeneity of the material were investigated using a Zeiss Leo 1550 field emission SEM equipped with an Aztec energy dispersive X-ray detector (EDS). The data were collected using a powder sample attached to conducting carbon tape and the spectra were collected at 20 different points using an accelerating voltage of 20 kV. Additionally, EDS maps were measured to investigate the homogeneity of the sample.

2.4. Magnetism

Isothermal magnetization curves were measured at various temperatures down to 6 K using a Quantum Design MPMS XL and at and above room temperature (RT) using a LakeShore 7400 series VSM equipped with a furnace. Magnetization versus temperature measurements were conducted using an applied field of 8 kA/m (0.01 T) up to 600 K at a rate of 1 K/min.

2.5. Electronic structure calculations

The electronic structure was investigated by solving the Kohn-Sham equations as implemented in the spin-polarized relativistic

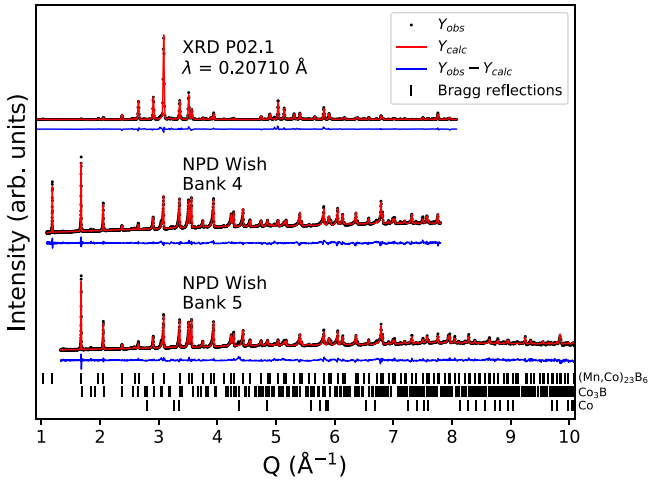

Fig. 2. Measured and calculated diffraction patterns from joint refinement using data from P02.1 and two detector banks from Wish at 700 K. Total χ^2 = 9.29, R_{Bragg} = 7.95, 3.14 and 2.83 for the P02.1, banks 5 and 4, respectively.

Korringa-Kohn-Rostoker (SPR-KKR) code [26]. The chemical disorder was treated within the coherent potential approximation [27,28]. The Vosko-Wilk-Nusair [29] version of the local spin density approximation was employed as exchange-correlation functional. The scalar relativistic calculations were performed using the atomic sphere approximation for the shape of the external potential. The angular momentum cutoff of l_{max} = 3 was used in the multiple scattering expansion. A *k*-point grid consisting of ≈ 250 points in the irreducible Brillouin zone was employed for the self-consistent calculations, and ≈ 1250 points for the density of state (DOS) and magnetic exchange interaction (J_{ij}) calculations. The exchange parameters J_{ij} between the atomic magnetic moments were calculated using the Liechtenstein-Katsnelson-Antropov-Gubanov formalism [30,31]. The Curie temperature was evaluated within the mean-field approximation [32] for ferromagnetic and ferrimagnetic reference states.

3. Results and discussion

3.1. Crystallographic properties

To understand the magnetic interactions in the $(Mn,Co)_{23}B_6$ compound, the nuclear structure needs to be explored fully. Due to the similar electron densities of Mn and Co, giving similar scattering power for X-rays, a combination of XRD and NPD was employed for this determination. At 700 K, the sample is in a paramagnetic state (see the magnetic properties section below) and thus the NPD patterns should only contain information about the nuclear structure. Therefore, a joint crystal structure refinement with data from P02.1 at DESY and the two detector banks (5 and 4) with the highest resolution from Wish at ISIS was performed, Figure 2. The refinement revealed that the purity of the $(Mn,Co)_{23}B_6$, SG $Fm\bar{3}m$, phase is ~ 94 wt%, with two secondary phases, Co_3B, SG *Pnma*, (~ 5 wt%) and Co, SG $P6_3/mmc$, (~ 1 wt%). For the main phase, $(Mn,Co)_{23}B_6$, unit cell parameters, atomic positions, thermal displacement parameters (B_{iso}) as well as the occupancy could be refined. The atomic positions and B_{iso} parameters were restricted to take the same values for each crystallographic site. The occupancies on each site were refined independently but restricted so that all atomic positions were fully occupied. The refined parameters are summarized in Table 1, and show a clear preference for Co at the 48*h* and 32*f* positions whereas Mn prefers the 8*c* position and the occupancy at the 4*a* position is equal. The cubic unit cell parameter *a* was refined to 10.5873(3) Åat 700 K. The total composition of the phase calculated from the refinement is Mn-rich ($Mn_{4.7}Co_{18.3}B_6$) as compared to the nominal composition. However, the exact composition is challenging to refine due to mixed occupancies on all metallic sites. Instead the composition of the sample was verified by independent composition measurements using EDS, which indicated smaller Mn-excess ($Mn_{3.23}Co_{19.77}$), with standard deviations of less than 2 at%, and in good agreement with the nominal composition. EDS mapping (shown in the supporting information (SI), Figure S1) of the powdered sample suggested good homogeneity and an even distribution of Co/Mn over the areas studied.

During the NPD experiment the sample was heated to 700 K, cooled to 6 K and then heated again to RT. The temperature 700 K is a high enough temperature that solid state diffusion could possibly occur and therefore measurements were done at start and end of the experiment to ensure that no structural changes occurred during the heating. The resulting NPD patterns from bank 2 are shown in Figure S2 and shows identical diffraction patterns. This means that no diffusion at any detectable level has occurred during the experiment and also shows that the refined nuclear structure model can be used for refinements of magnetic structures to the low temperature diffraction data. This further shows that the studied compound is stable up to at least 700 K.

3.2. Magnetic properties

The experimentally obtained results from magnetometry for $(Mn,Co)_{23}B_6$ are summarized in Figure 3. Referring to the magnetization curves at 6 K and 300 K in Figure 3(a) it is found that an applied magnetic field of 5T is enough to saturate the sample. The magnetic moment decreases from 20.1 μ_B/f.u. at 6 K to 17.7 μ_B/f.u. at 300 K. These magnetic moments per formula units are in later sections compared to magnetic moments calculated from Rietveld refinements of neutron powder diffraction data as well as electronic structure calculations. The low field magnetization results presented in Figure 3(b) are essentially featureless from room temperature down to 6 K, indicating that no complex magnetic ordering occurs in that temperature range. This featureless magnetization versus temperature curve is essential for a correct description of the magnetic structure from NPD. Heating the sample slowly up to 600 K yields T_C = 550 K with minimal thermal hysteresis, where T_C is taken

Table 1
Refined atomic positions from the joint refinement at 700 K for $(Mn,Co)_{23}B_6$. Standard error is given within the parenthesis. *a* = 10.5873(3) Å.

Atom	Wyckoff position	*x*	*y*	*z*	Occupancy	B_{iso} (Å^2)
B	24*e*	0.2743(3)	0	0	1	1.81(2)
Co1	48*h*	0	0.1701(4)	0.1701(4)	0.878(5)	1.04(2)
Mn1	48*h*	0	0.1701(4)	0.1701(4)	0.122(5)	1.04(2)
Co2	32*f*	0.3828(4)	0.3828(4)	0.3828(4)	0.878(5)	0.76(1)
Mn2	32*f*	0.3828(4)	0.3828(4)	0.3828(4)	0.122(5)	0.76(1)
Mn3	8*c*	0.25	0.25	0.25	0.800(4)	1.55(3)
Co3	8*c*	0.25	0.25	0.25	0.200(4)	1.55(3)
Mn4	4*a*	0	0	0	0.507(3)	1.44(6)
Co4	4*a*	0	0	0	0.493(3)	1.44(6)

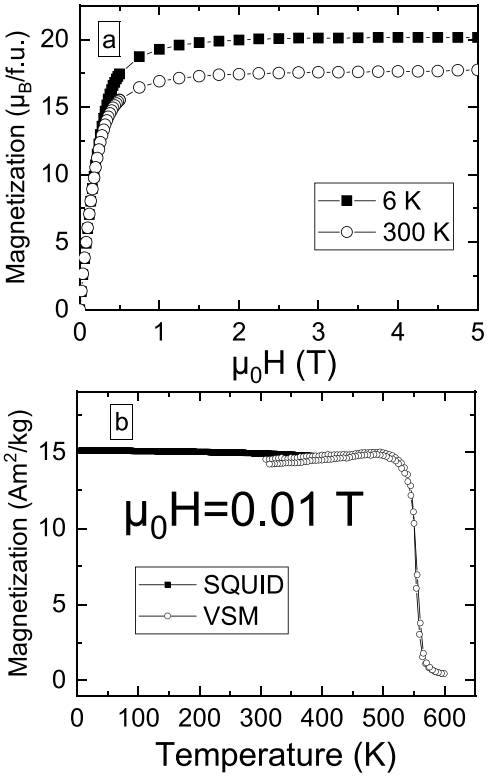

Fig. 3. (a) Magnetization in μ_B/f.u versus applied field at 6 K yielding a saturation magnetization of 20.1 μ_B/f.u. (black filled rectangles), which decreases to 17.7 μ_B/f.u at 300 K. (open circles). (b) Magnetization versus temperature in an applied field μ_0H = 0.01 T. Black filled rectangles refers to data collected with the Quantum Design MPMS XL system while the white open circles are data collected in the LakeShore 7400 series VSM.

from the inflection point of the dM/dT curve. As can be seen in SI, magnetic hysteresis curves collected before and after heating show minimal changes (< 0.1%) in for instance saturation magnetization.

3.3. Magnetic structure

To investigate the magnetic structure, NPD was carried out at 6 K. When comparing the diffraction patterns at 6 K and 700 K an increase in the intensity of several reflections is observed, which is an effect of the magnetic ordering, shown in Figure S3. Increased intensities at existing reflections, and nowhere else, indicate that the propagation vector **k** = (0 0 0) can be used. Using the structural information and the propagation vector, potential magnetic space groups (MSGs) with non-zero magnetic moments were investigated using BCS and the tool k-SUBGROUPSMAG [24]. This resulted in a number of possible MSGs that could describe the magnetic structure for $(Mn,Co)_{23}B_6$. All the possible magnetic subgroups are visualized in SI. The three MSGs with the highest symmetries, $I4/mm'm'$, $Im'm'm$ and $R\bar{3}m'$, were selected for further testing. It is worth to note that these three MSGs are subgroups that can be the result of a Landau-type transition, i.e. coming from a single irreducible representation. Figure 4 shows the obtained data and the refined model with MSG $I4/mm'm'$ at 6 K. Upon performing refinements of the three different models, similar, but not identical, magnetic structure models were obtained. All models are ferrimagnetic, yielding magnetic moments per formula unit that are in line with the magnetometry results. In the models, the metal atom on the 4*a*-position aligns oppositely to all other metal atoms. However, the directions of the magnetic moments vary between the different MSGs. Since the different magnetic models have similar agreement factors and number of refined parameters, the difference in the

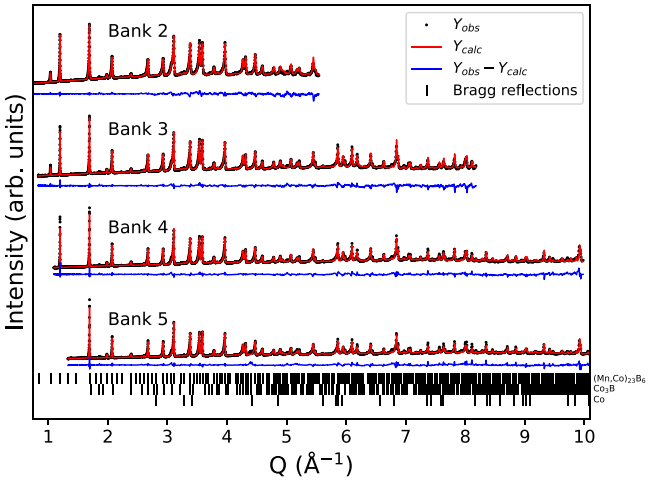

Fig. 4. Measured and calculated multi-histogram diffraction patterns of the magnetic structure model $I4/mm'm'$ at 6 K. R_{Bragg} = 3.87, 3.81, 3.60 and 3.10 for the banks 5, 4, 3 and 2, respectively. The R_{Mag}-values are all comparable to R_{Bragg}.

MSGs can be found in their symmetries. As the MSG model $I4/mm'm'$ has the highest symmetry, it is the preferred magnetic structure model and is the one shown in Figure 5 and Table 2. The transformation from the cubic space group $Fm\bar{3}m$ to the tetragonal setting is performed using $((\frac{1}{2})a + (\frac{1}{2})b, -(\frac{1}{2})a + (\frac{1}{2})b, c; 0, 0, 0)$ and gives rise to a splitting of the metal position at 48*h* (Co1 in Table 1). The refined magnetic moments are all along the crystallographic *c*-direction in the cubic symmetry, and of a different sign for the 4*a*-site. The total magnetic moment from the refinement is 18.2 μ_B/f.u. at 6 K, which is in good agreement with the moment observed from the magnetometry. The moment size on e.g. Co2 and Mn4 is smaller than expected. However, the intermixing of Co and Mn on all sites makes it seems probable that there is competition of ferro- and antiferromagnetic interactions, giving a smaller net magnetic moment. Due to the nature of diffraction analysis, the magnetic moments cannot be resolved for each element, yielding only an average for the different crystallographic sites.

As the magnetic structure model presented here is not the only unique solution to explain the magnetic behavior, further research is

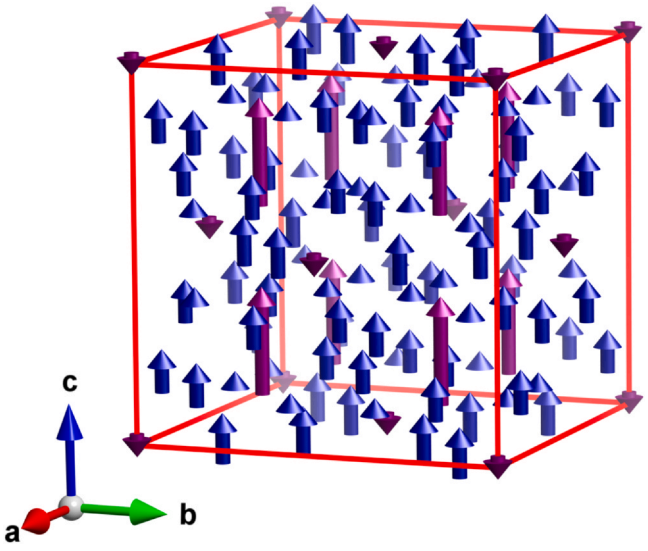

Fig. 5. Refined magnetic structure model for $(Mn,Co)_{23}B_6$ using the MSG $I4/mm'm'$ with the moments of the cobalt- and manganese-rich sites depicted with blue and purple arrows, respectively.

Table 2
Refined atomic positions and magnetic moments along the c-direction from the refinement at 6 K for the metal positions. Standard error is given within parenthesis. a = 10.5022(3) Å. Last two columns list the magnetic moments for each Wyckoff position, i.e. $m_{site} = \sum_i c_i m_i$, calculated for the $Fm\bar{3}m$ and $I4/mm'm'$ structures, respectively. c_i are given by the occupancy of each position from Table 1.

Atom	Wyckoff position	x	y	z	Magnetic moment (μ_B)	$m_{site} Fm\bar{3}m$ (μ_B)	$m_{site} I4/mm'm'$ (μ_B)
Co1(1)	48h	0	0.1695(4)	0.1695(4)	0.90(3)	1.36	1.27
Co1(2)	48h	0.1695(4)	0.1695(4)	0	1.04(5)		1.27
Co2	32f	0.3826(1)	0.3826(1)	0.3826(1)	0.36(3)	1.10	0.74
Mn3	8c	0.25	0.25	0.25	2.22(6)	2.42	2.06
Mn4	4a	0	0	0	-0.48(5)	-0.65	-0.57

needed to resolve this ambiguity. This would require single crystals of this compound to be synthesized.

3.4. Electronic structure and magnetic properties

Electronic structure and magnetic properties were studied for the refined nuclear structure with SG $Fm\bar{3}m$ (cubic symmetry, crystallographic data listed in Table 1) as well as for the possible magnetic structures with MSGs $I4/mm'm'$ (tetragonal symmetry, crystallographic data listed in Table S2), $Im'm'm$ and $R\bar{3}m'$ (crystallographic data listed in Table S3 and S4, respectively), by means of density functional theory. The density of states (DOS) of cubic $(Mn,Co)_{23}B_6$ with the $Fm\bar{3}m$ is plotted with black lines in Figure 6. The system is metallic with a large number of states at the Fermi energy. States at the −6–0 eV energy range mainly consist of hybridized Co and Mn 3d states, while B s, and Co and Mn s and p states build the smaller DOS peak around −8 eV. The energy shift of the spin up and spin down states results in a magnetic moment of 28.57 μ_B/f.u. DOS for the experimentally attained magnetic structures are also plotted in Figure 6. These DOSs are almost identical with minor differences leading to a small reduction of the magnetic moment per formula unit calculated for the $I4/mm'm'$, $Im'm'm$ and $R\bar{3}m'$ symmetries (24.1, 27.0 and 24.6 μ_B/f.u., respectively) compared to that calculated for the $Fm\bar{3}m$ (28.57 μ_B/f.u.).

Element and site resolved magnetic moments are listed in Table 2 for the refined nuclear structure described by the $Fm\bar{3}m$ space group (cubic symmetry) and for the refined magnetic structure with $I4/mm'm'$(tetragonal symmetry) for comparison to the experimental data. They are defined as the weighted average of the element resolved local moments (m_i) for a given site, i.e., $m_{site} = \sum_i c_i m_i$. c_i is given by the occupancy of each position found in Tables 1 and S2. The 0 K theoretical values for m_{site} are larger then those obtained by NPD measurements. For the cubic symmetry, $Fm\bar{3}m$, the large difference between the magnetic moments of different Wyckoff positions mainly occupied by Co, i.e. 48h and 32f, respectively, is not seen (Table 2). This will result in a considerably higher calculated magnetization per formula unit compared to the measured one. The difference between calculated and experimental moments is smaller for positions mainly occupied by Mn atoms, i.e., 8c and 4a, respectively. The sign of the moment on the 4a site is captured well when the $Fm\bar{3}m$ symmetry is applied in the calculations, but the magnitude is too high. The negative sign is a consequence of the antiparallel alignment of Mn to Co. Mn has −3.25 μ_B local moment, while Co possess 1.94 μ_B local moment.

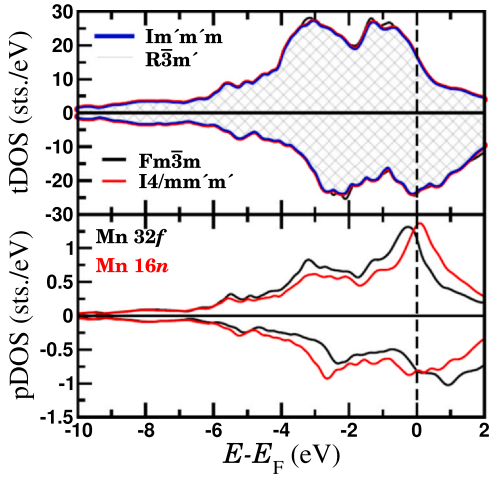

Fig. 6. Upper panel: Total density of states for the refined nuclear structure with $Fm\bar{3}m$ symmetry plotted with black lines, and for the refined magnetic structures $I4/mm'm'$ and $Im'm'm$ plotted with red and blue lines, respectively, together with DOS for the $R\bar{3}m'$ symmetry represented by the gray shaded area. Vertical dashed black line indicates the Fermi level. Note, that DOS for the magnetic structures are very similar and they overlap considerably. Lower panel: Element resolved partial DOS for Mn occupying the 32f ($Fm\bar{3}m$ symmetry, black line) and 16n ($I4/mm'm'$, red line) positions.

The best theoretical description for the magnetic properties is given by the $I4/mm'm'$ tetragonal symmetry assuming a ferrimagnetic state when Mn atoms in the 4a position orient antiparallel to the rest of the local moments. The calculated m_{site} listed in Table 2 are larger than the measured moments, this results in a larger average magnetic moment per f.u. compared to the experimental data but smaller than for the $Fm\bar{3}m$ symmetry. Site and element resolved magnetic moments and corresponding Wyckoff positions for the cubic and tetragonal symmetries are listed in Table 3. The large difference between moments on 48h (16m + 8i) position and 32f (16n) positions is well captured for the tetragonal symmetry, in contrast to the finding for the cubic case. The symmetry change results in the modification of both Co and Mn local moments on the 32f positions. In the cubic symmetry, both Co and Mn local moments are large and positive for both the 48h and 32f positions (Table 3). The Co moments on the 48h position decrease for $I4/mm'm'$ compared to the $Fm\bar{3}m$ symmetry. For Mn, the local moment on 32f is large and positive while on the 16n position it becomes smaller and negative. This is a consequence of the migration of electrons from the spin-up channel to the spin-down channel plotted in the lower panel of Figure 6. Therefore, m_{site} on the 32f (16n) position becomes considerably smaller in the tetragonal description than in the cubic symmetry, resulting in a better agreement between the calculated data and the measured data. For 8c (4d) and 4a (2a), both Co and Mn local moments decrease with reduced symmetry.

Table 3
Element and site resolved magnetic moments (m) calculated for the refined nuclear and magnetic structures, respectively.

Atom	Wyckoff position $Fm\bar{3}m$	m (μ_B)	Atom	Wyckoff position $I4/mm'm'$	m (μ_B)
Co1	48h	1.26	Co1(1)	16m	1.18
Mn1	48h	2.10	Mn1(1)	16m	1.89
			Co1(2)	8i	1.18
			Mn1(2)	8i	1.89
Co2	32f	1.04	Co2	16n	0.88
Mn2	32f	1.57	Mn2	16n	-0.26
Mn3	8c	2.60	Mn3	4d	2.14
Co3	8c	1.72	Co3	4d	1.65
Mn4	4a	-3.25	Mn4	2a	-3.03
Co4	4a	1.94	Co4	2a	1.89

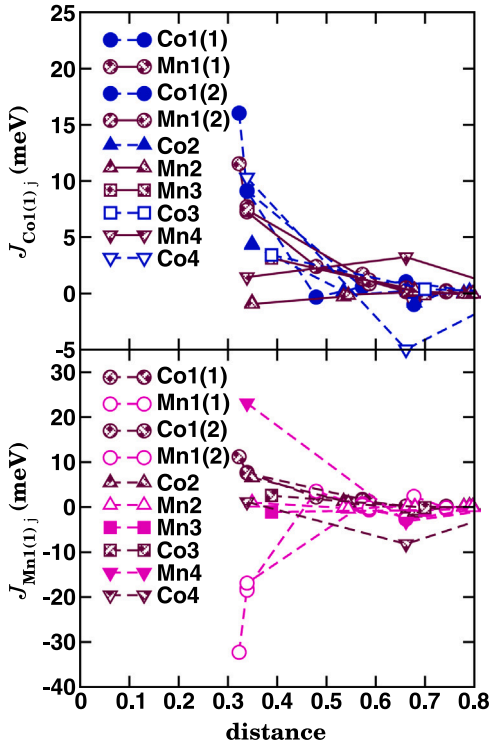

Fig. 7. Magnetic exchange interactions J_{ij} as a function of distance expressed in units of lattice parameter a for disordered $(Mn,Co)_{23}B_6$ in the MSG $I4/mm'm'$. Full symbols represent atoms with high occupation on their own positions, while empty symbols belong to atoms with low occupation number. Blue stands for J_{ij} between Co atoms, magenta stands for J_{ij} between Mn atoms and shaded maroon stands for $J_{Co\text{-}Mn}$ ($J_{Mn\text{-}Co}$).

Element resolved partial density of states plotted for Mn in the lower panel of Figure 6 reveals that the difference between the local magnetization of Mn in the tetragonal symmetry compared to the cubic symmetry is a consequence of the large shift of the electron population towards the spin-down channel for the tetragonal symmetry. As is visible, the spin-up channel in the cubic symmetry is more populated than the spin-down channel. For example there is a peak around − 3 eV as well as right below the Fermi level in the spin-up channel, while, in the spin-down channel, the lower lying peak moves towards higher energy and the Fermi level is situated well below the peak nearby. This distribution of the electrons between the energy channels will result in a large positive m_{Mn} on the 32*f* position. Contrary, in the spin-up channel of the tetragonal symmetry, the peak around − 3 eV lowers and also the Fermi level moves below the peak. The spin-down channel however gets more populated, resulting in a small negative m_{Mn} on the 16*n* position. For other positions there is not as large a change in the DOS by lowering the symmetry (see Figures S8 and S9).

The most representative magnetic exchange coupling constants J_{ij} between the metallic elements are plotted in Figure 7 for $I4/mm'm'$ tetragonal symmetry. Co (Mn) atoms occupying 16*m*, 8*i* and 16*n* high multiplicity positions with high (low) occupation number are labeled as Co1(1) (Mn1(1)), Co1(2) (Mn1(2)) and Co2 (Mn2), respectively, while Mn (Co) atoms occupying 4*d* and 2*a* low multiplicity positions with high (low) occupation number are labeled as Mn3 (Co3) and Mn4 (Co4), respectively. Co1(1) couples with medium strength (10–20 meV) positive coupling to all Co atoms (cf. Figure 7). $J_{Co1(2)_j}$ and J_{Co2_j} are similar to $J_{Co1(1)_j}$ (see Figures S10 and S11). J_{Co3Co3}, J_{Co3Co4}, and J_{Co4Co4} are positive and small (< 5 meV) compared to the other interactions (shown in Figures S12 and S13). The J_{CoMn} interactions are comparable in magnitude with the J_{CoCo} interactions. Co1(1), Co1(2), Co2 and Mn atoms in 16*m* (Mn1(1)), 8*i* (Mn1(2)) and 8*c* (Mn3) positions (Figures 7, S10 and S11) couple with a medium strength positive coupling. J_{CoMn2} is small and negative, while J_{Co1Mn4} is small and positive and $J_{Co2,3Mn4}$ are small and negative. J_{Co4Mn} (plotted in Figure S13) is similar to J_{Co3Mn}. The largest positive couplings (> 20 meV) are found between Mn atoms in 16*m* (Mn1(1)), 8*i* (Mn1(2)) and Mn4 positions, $J_{Mn1(1)Mn4}$, $J_{Mn1(2)Mn4}$, J_{Mn2Mn4}, shown in Figures 7, S14 and S15. J_{Mn2Mn3} are medium strength and positive, while J_{Mn2Mn2}, J_{Mn2Mn4}, J_{Mn3Mn4} and J_{Mn4Mn4} are around 1–2 meV. $J_{Mn1(1)Mn1(1)}$, $J_{Mn1(1)Mn1(2)}$ and $J_{Mn1(2)Mn1(2)}$ (Figure S14) are the strongest interactions and are negative (−30 meV). J_{ij} for Mn3 and Mn4 are plotted on Figures S16 and S17.

In the classical Heisenberg model the magnetic energy H is defined as $H = -\sum_{ij} J_{ij}\,\vec{e}_i\,\vec{e}_j$, where J_{ij} is the exchange coupling constant and $\vec{e}_i$ and $\vec{e}_j$ are the unit vectors characterizing the orientation of the magnetic moments for atom i and j, respectively. By definition a positive J_{ij} means ferromagnetic coupling, i.e. stabilizes the ferromagnetic solution. Keeping in mind the multiplicity and occupancy of all positions and that all Co atoms and Mn1, Mn3 atoms possess positive moments, and Mn2 and Mn4 possess negative moments, the following conclusions can be made. All J_{CoCo}, J_{CoMn1}, J_{CoMn3} (where both J_{ij} and $m_i > 0$) will establish a ferromagnetic solution for the Heisenberg Hamiltonian of the $(Mn,Co)_{23}B_6$ system. J_{CoMn2} will lower the energy stabilizing the antiparallel alignment of Mn2 ($J_{ij} < 0$). J_{CoMn4} increases the magnetic energy ($(J_{ij} > 0, \vec{e}_i = +1, \vec{e}_j = -1$), but the magnitude is small, so this effect is negligible. This is also the case for all J_{Co4Co} and J_{Co4Mn}. All J_{MnMn} (where either $J_{ij} > 0$ and $\vec{e}_i = -1$, $\vec{e}_j = +1$ or $J_{ij} < 0$ and $\vec{e}_i$, $\vec{e}_j = +1$) and J_{CoMn4} and J_{CoMn2} (where $J_{ij} > 0$ and $\vec{e}_i = -1$, $\vec{e}_j = +1$) will increase the magnetic energy for the ferrimagnetic configuration of $(Mn,Co)_{23}B_6$ system. These effects result in a higher energy for ferrimagnetic $(Mn,Co)_{23}B_6$ compared to the ferromagnetic solution.

To shed more light on the magnetic properties of $(Mn,Co)_{23}B_6$ system, total energy calculations have been performed for the experimental composition and for a partially ordered $(Mn,Co)_{23}B_6$, with Co occupying 100% the 48*h* (16*m* + 8*i*) and 32*f* (16*n*) positions, 50% Co on the 4*a* position, while Mn fully occupies the 8*c* position and 50% Mn is present on the 4*a* position, in different magnetic states. The total energy difference is defined as $\Delta E = E_{ferrimagnetic} - E_{ferromagnetic}$. Here $E_{ferrimagnetic}$ corresponds to a magnetic state where the magnetic moment of Mn4 (m_{Mn4}) is antiparallel to other magnetic moments, in agreement with the experimental findings, while $E_{ferromagnetic}$ corresponds to a magnetic state where m_{Mn4} is parallel to other local moments. The total energy differences listed in Table 4 show that for the partially ordered (Mn,Co)23B6 the ferrimagnetic solution has lower energy compared to the ferromagnetic state regardless of the symmetry. In contrast, for the experimental chemical arrangement, i.e., Mn-Co intermixing on the Co main positions, the total energy difference ΔE decreases compared to the partially ordered case in the cubic symmetry. That means that the ferrimagnetic solution is less stable for the disordered phase than for the partially ordered case. For the tetragonal symmetry, the ferromagnetic solution gets the lowest energy for the disordered phase. Analysis of J_{ij}s for partially ordered $(Mn,Co)_{23}B_6$, reveal that without the destabilizing effect of the large negative coupling exhibited by Mn "impurities" on the Co positions, $(Mn,Co)_{23}B_6$ becomes ferrimagnetic where Mn on the 4*a* position has an opposite alignment

Table 4
Total energy differences in mRy/f.u. calculated at 0 K, i.e. $\Delta E = E_{ferrimagnetic} - E_{ferromagnetic}$, for different magnetic solutions of the cubic ($Fm\bar{3}m$) and tetragonal ($I4/mm'm'$) structures. Negative values correspond to the case where the ferrimagnetic solution has lower energy.

ΔE	$Fm\bar{3}m$ (cubic)	$I4/mm'm'$ (tetragonal)
partially ordered	-5.8	-8.1
disordered	-5.2	13.9

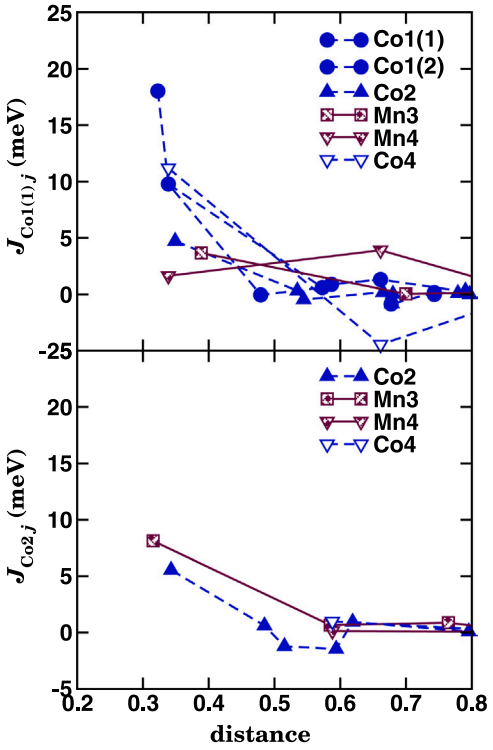

Fig. 8. Magnetic exchange interactions J_{ij} of Co-Co and Co-Mn atoms in the partially ordered $(Mn,Co)_{23}B_6$ in the $I4/mm'm'$ symmetry. Blue stands for J_{ij} between Co atoms, and shaded maroon stands for $J_{Co\text{-}Mn}$ ($J_{Mn\text{-}Co}$).

Table 5
Mean-field estimates of the Curie temperatures (T_C) for different magnetic solutions of the cubic ($Fm\bar{3}m$) and tetragonal ($I4/mm'm'$) structures.

	$Fm\bar{3}m$ (cubic)		$I4/mm'm'$ (tetragonal)	
T_C	ferro	ferri	ferro	ferri
partially ordered	801	773	748	741
disordered	738	727	626	612

compared to the other atoms. J_{CoCo} and J_{CoMn} interactions, plotted in Figure 8, are affected by ordering only in the magnitude within 1–3 meV range. Mn-Mn interactions are very small and are plotted on Figures S19 and S20.

The magnetic transition temperatures, T_C, are estimated using the mean-field approximation for ferromagnetic and ferrimagnetic configurations with both cubic and tetragonal structures. The obtained data are listed in Table 5. Observations show that the different magnetic configurations have less effect on the Curie temperature than chemical ordering. The antiparallel coupling of Mn atoms in the 4*a* position stabilizes the ferrimagnetic state of partially ordered $(Mn,Co)_{23}B_6$ resulting in an increase of the magnetic transition temperature by 100 K. In case of disordered $(Mn,Co)_{23}B_6$ the antiparallel coupling of Mn atoms in the 4*a* position destabilizes both the ferromagnetic and ferrimagnetic solution, therefore the magnetic transition temperature is lower.

4. Conclusion

In this study a compound in the $(Mn,Co)_{23}B_6$-system has been successfully synthesized via a high temperature solid-state powder route. It crystallizes in the cubic space group $Fm\bar{3}m$, with intermixing of Mn and Co at four crystallographic sites. Combination of synchrotron X-ray and neutron diffraction at 700 K revealed that there is a partial ordering of the metals with Co- and Mn-rich positions. Magnetometry revealed a magnetic transition at 550 K upon heating, with no additional magnetic transitions at lower temperatures, and a saturated magnetic moment of 20.1 μ_B/f.u. at 6 K. The magnetic structure was evaluated with neutron diffraction which revealed a ferrimagnetic ordering along the crystallographic *c*-direction in the magnetic space group $I4/mm'm'$. The magnetic moments in the corner positions align in the opposite direction compared to magnetic moments in other positions. The total magnetic moment was refined to 18.2 μ_B/f.u., which is in good agreement with the magnetometry value. First principles calculations support the ferrimagnetic state for an ordered $(Mn,Co)_{23}B_6$. However, when 10% Mn is accommodated on the Co main sites, 0 K calculations reveal a ferromagnetic ground state with larger average magnetization compared to the measured ones for the $I4/mm'm'$ symmetry. The discrepancy between measured and calculated magnetic moments may be resolved by establishing a ferrimagnetic magnetic configuration for the theoretical model that applies to the $I4/mm'm'$ symmetry. The use of Mn impurities to destabilize a ferrimagnetic state in favor of a ferromagnetic one remains an interesting prospect within the field of magnetism. It could potentially be an avenue to further improve functional properties of magnetic materials.

CRediT authorship contribution statement

Simon R. Larsen: Investigation, Writing – original draft, **Daniel Hedlund:** Investigation, Writing – original draft, **Rebecca Clulow:** Investigation, Writing – original draft, **Martin Sahlberg:** Conceptualization, Data curation, Methodology, Project administration, Writing – review & editing, **Peter Svedlindh:** Conceptualization, Data curation, Methodology, Project administration, Writing – review & editing, **Erna K. Delczeg-Czirjak:** Investigation, Data curation, Writing – original draft, **Johan Cedervall:** Conceptualization, Data curation, Methodology, Project administration, Writing – original draft.

Declaration of Competing Interest

The authors declare the following financial interests/personal relationships which may be considered as potential competing interests:Simon Rosenqvist Larsen reports equipment, drugs, or supplies was provided by ISIS Pulsed Neutron and Muon Source. Simon Rosenqvist Larsen reports equipment, drugs, or supplies was provided by German Electron-Synchrotron.

Acknowledgments

The authors thank the Swedish Research Council (VR) and the Swedish Foundation for Strategic Research (SSF), project "Magnetic materials for green energy technology" (contract EM-16-0039) for financing this project. We acknowledge DESY (Hamburg, Germany), a member of the Helmholtz Association HGF, for the provision of experimental facilities. Parts of this research were carried out at Petra III and we would like to thank Dr. Christian Kolle Christensen for assistance in using the beamline P02.1. Experiments at the ISIS Neutron and Muon Source were supported by a beamtime allocation RB1920041 from the Science and Technology Facilities Council. The authors also wish to thank Dr. Pascal Manuel for the help provided during the neutron diffraction beamtime. E.K.D-Cz. acknowledges STandUPP and eSSENCE for financial support and the Swedish National Infrastructure for Computing (SNIC) for computational resources.

Appendix A. Supporting information

Supplementary data associated with this article can be found in the online version at doi:10.1016/j.jallcom.2022.164225.

References

[1] O. Gutfleisch, M.A. Willard, E. Brück, C.H. Chen, S.G. Sankar, J.P. Liu, Magnetic materials and devices for the 21st century: stronger, lighter, and more energy efficient, Adv. Mater. 23 (7) (2011) 821–842, https://doi.org/10.1002/adma.201002180

[2] A. Westgren, Complex chromium and iron carbides, Nature 132 (3334) (1933), https://doi.org/10.1038/132480a0 (480–480).

[3] X.X. Wei, W. Xu, J.L. Kang, M. Ferry, J.F. Li, Metastable Co_{23} B_6 phase solidified from deeply undercooled $Co_{79.3}$ $B_{20.7}$ alloy melt, J. Mater. Sci. 51 (13) (2016) 6436–6443, https://doi.org/10.1007/s10853-016-9941-4

[4] D. Kotzott, M. Ade, H. Hillebrecht, Single crystal studies on Co-containing τ -borides Co_{23-x} M_x B_6 (M = Al, Ga, Sn, Ti, V, Ir) and the boron-rich τ -boride $Co_{12.3}$ $Ir_{8.9}$ $B_{10.5}$, J. Solids . Chem. 182 (3) (2009) 538–546, https://doi.org/10.1016/j.jssc.2008.10.036

[5] H. Hillebrecht, M. Ade, B_4 tetrahedra for aluminum — a surprising substitution in τ -Borides Ni_{20} Al_3 B_6 and Ni_{20} AlB_{14}, Angew. Chem. Int. Ed. 37 (7) (1998) 935–938, https://doi.org/10.1002/(SICI)1521-3773(19980420)37:7<935::AID-ANIE935>3.0.CO;2-0

[6] H. Hirota, Magnetic properties of borides with a Cr_{23} C_6 structure, J. Phys. Soc. Jpn. 23 (3) (1967) 512–516, https://doi.org/10.1143/JPSJ.23.512

[7] V. Keimes, A. Mewis, Mg_3 Ni_{20} P_6 und Mn_3 Ni_{20} P_6 - Zwei neue phosphide mit Cr_{23} C_6 -Struktur, Z. für Anorg. Allg. Chem. 618 (12) (1992) 35–38, https://doi.org/10.1002/zaac.19926180107

[8] T. Eriksson, M. Vennström, S. Ronneteg, Y. Andersson, P. Nordblad, Complex magnetic properties of Mn_3 Ni_{20} P_6 and ferromagnetic structure of the new isostructural compound Mn_3 Pd_{20} P_6, J. Magn. and Magn. Mater. 308 (2) (2007) 203–209, https://doi.org/10.1016/j.jmmm.2006.05.016

[9] J. Cedervall, P. Beran, M. Vennström, T. Danielsson, S. Ronneteg, V. Höglin, D. Lindell, O. Eriksson, G. André, Y. Andersson, P. Nordblad, M. Sahlberg, Low temperature magneto-structural transitions in Mn_3 Ni_{20} P_6, J. Solid State Chem. 237 (2016) 343–348, https://doi.org/10.1016/j.jssc.2016.02.028

[10] T. Herrmannsdörfer, A. Dönni, P. Fischer, L. Keller, G. Böttger, M. Gutmann, H. Kitazawa, J. Tang, Successive magnetic ordering of the Tb sublattices in Tb_3 Pd_{20} Si_6, J. Phys. Matter 11 (14) (1999) 2929–2936, https://doi.org/10.1088/0953-8984/11/14/009

[11] T. Herrmannsdörfer, A. Dönni, P. Fischer, L. Keller, H. Kitazawa, Two successive magnetic phase transitions in Dy_3 Pd_{20} Si_6 studied by neutron powder diffraction, Phys. B: Condens. Matter 281-282 (2000) 167–168, https://doi.org/10.1016/S0921-4526(99)01213-2

[12] J. Kitagawa, N. Takeda, M. Ishikawa, Low-temperature magnetic properties of $(RE)_3$ Pd_{20} Si_6 (RE = La to Yb), J. Alloy. Compd. 256 (1–2) (1997) 48–56, https://doi.org/10.1016/S0925-8388(96)03020-4

[13] A. Dönni, F. Fauth, P. Fischer, T. Herrmannsdörfer, L. Keller, T. Komatsubara, Sample quality and the magnetic phase transitions in Nd_3 Pd_{20} Ge_6: neutron diffraction study, J. Alloy. and Compd. 306 (2000) 40–46, https://doi.org/10.1016/S0925-8388(00)00769-6

[14] Y.B. Kuz'ma, M.V. Chepiga, A.M. Plakhina, Phase equilibria in the Cr-Co-B, Mn-Fe-B, and Mn-Co-B systems, Inorg. Mater. 2 (7) (1966) 1038–1043.

[15] G. Pradelli, C. Gianoglio, E. Quadrini, Ricerca sui boruri di cobalto e manganese, Metall. Ital. 70 (1978) 122–126.

[16] A. Burdese, G. Pradelli, C. Gianoglio, Struttura parzialmente ordinata di fasi complesse del tipo Cr_{23} C_6, Metall. Ital. 69 (1977) 487–492.

[17] A.-C. Dippel, H.-P. Liermann, J.T. Delitz, P. Walter, H. Schulte-Schrepping, O.H. Seeck, H. Franz, Beamline P02.1 at PETRA III for high-resolution and high-energy powder diffraction, J. Synchrotron Radiat. 22 (3) (2015) 675–687, https://doi.org/10.1107/S1600577515002222

[18] V. Höglin, J. Ångström, M.S. Andersson, O. Balmes, P. Nordblad, M. Sahlberg, Sample cell for in-field x-ray diffraction experiments, Result. Phys. 5 (2015) 53–54, https://doi.org/10.1016/j.rinp.2015.01.006

[19] A.P. Hammersley, S.O. Svensson, M. Hanfland, A.N. Fitch, D. Hausermann, Two-dimensional detector software: from real detector to idealised image or two-theta scan, High. Press. Res. 14 (4–6) (1996) 235–248, https://doi.org/10.1080/08957959608201408

[20] L.C. Chapon, P. Manuel, P.G. Radaelli, C. Benson, L. Perrott, S. Ansell, N.J. Rhodes, D. Raspino, D. Duxbury, E. Spill, Wish: The new powder and single crystal magnetic diffractometer on the second target station, Neutron N. 22 (2) (2011) 22–25, https://doi.org/10.1080/10448632.2011.569650

[21] J. Cedervall, P. Manuel, S. R. Larsen, M. Sahlberg, Magnetic structure determinations in the complex boride Mn3 Co20 B6, STFC ISIS Neutronand Muon Source (2019) 10.5286/ISIS.E.RB1920041.

[22] H.M. Rietveld, A profile refinement method for nuclear and magnetic structures, J. Appl. Crystallogr. 2 (2) (1969) 65–71, https://doi.org/10.1107/S0021889869006558

[23] J. Rodriguez-Carvajal, Recent advances in magnetic structure determination by neutron powder diffraction, Phys. B: Condens. Matter 192 (1–2) (1993) 55–69, https://doi.org/10.1016/0921-4526(93)90108-I

[24] J. Perez-Mato, S. Gallego, E. Tasci, L. Elcoro, G. de la Flor, M. Aroyo, Symmetry-based computational tools for magnetic crystallography, Annu. Mater. Res. 45 (1) (2015) 217–248, https://doi.org/10.1146/annurev-matsci-070214-021008

[25] K. Momma, F. Izumi, VESTA 3 for three-dimensional visualization of crystal, volumetric and morphology data, J. Appl. Crystallogr. 44 (6) (2011) 1272–1276, https://doi.org/10.1107/S0021889811038970

[26] H. Ebert, D. Ködderitzsch, J. Minár, Calculating condensed matter properties using the KKR-Green's function method-recent developments and applications, Rep. Prog. Phys. 74 (9) (2011) 096501.

[27] P. Soven, Coherent-potential model of substitutional disordered alloys, Phys. Rev. 156 (1967) 809–813, https://doi.org/10.1103/PhysRev.156.809

[28] G.M. Stocks, W.M. Temmerman, B.L. Gyorffy, Complete solution of the Korringa-Kohn-Rostoker Coherent-Potential-Approximation equations: Cu-Ni alloys, Phys. Rev. Lett. 41 (1978) 339–343, https://doi.org/10.1103/PhysRevLett.41.339

[29] S.H. Vosko, L. Wilk, M. Nusair, Accurate spin-dependent electron liquid correlation energies for local spin density calculations: a critical analysis, Can. J. Phys. 58 (8) (1980) 1200–1211, https://doi.org/10.1139/p80-159

[30] A. Liechtenstein, M. Katsnelson, V. Antropov, V. Gubanov, Local spin density functional approach to the theory of exchange interactions in ferromagnetic metals and alloys, J. Magn. Magn. Mater. 67 (1) (1987) 65–74, https://doi.org/10.1016/0304-8853(87)90721-9

[31] H. Ebert, S. Mankovsky, Anisotropic exchange coupling in diluted magnetic semiconductors: Ab initio spin-density functional theory, Phys. Rev. B79 (2009) 045209, https://doi.org/10.1103/PhysRevB.79.045209

[32] P.W. Anderson, Theory of magnetic exchange interactions: exchange in insulators and semiconductors, in: F. Seitz, Turnbull (Eds.), Solid State Physics, vol.14, Academic Press, New York, 1963.